Land use change as an anthropogenic driver of mercury pollution

Aryeh Feinberg[a], Martin Jiskra[b], Pasquale Borrelli[c], Jagannath Biswakarma[b,d], and Noelle E. Selin[a,e]

[a] *Institute for Data, Systems, and Society, Massachusetts Institute of Technology, Cambridge, MA, USA*

[b] *Environmental Geosciences, University of Basel, Basel, Switzerland*

[c] *Department of Science, Roma Tre University, Rome, Italy*

[d] *Department of Water Resources and Drinking Water, Eawag, Dübendorf, Switzerland*

[e] *Department of Earth, Atmospheric, and Planetary Sciences, Massachusetts Institute of Technology, Cambridge, MA, USA*

Correspondence to: arifeinberg@gmail.com (A.F.); martin.jiskra@gmail.com (M.J.)

Abstract

Mercury (Hg) released by anthropogenic activities can bioaccumulate to neurotoxic levels in commonly consumed fish[1–3]. Global soils are a global long-term storage for atmospheric Hg taken up by vegetation[4–6], thereby decreasing the Hg burden to oceans and eventually fish[7]. Anthropogenic activities like deforestation reduce the capacity of the terrestrial Hg sink[8] and enhance the release of Hg from soils through erosion[9] and volatilization[10,11]. However, the consequences of land use change on Hg cycling are not currently considered by anthropogenic emissions inventories or specifically addressed under the global Minamata Convention on Mercury[12]. Here, we use global atmospheric and erosion Hg models to investigate land use change impacts, focusing on Amazon deforestation and global-scale reforestation. Under a business-as-usual scenario[13] for Amazon deforestation in 2050, the Amazon sink of atmospheric Hg will be weakened by 65% compared to 2003 forest conditions, from 269 Mg yr^{-1} to 95 Mg yr^{-1}. Stricter conservation policies[13] prevent 92 Mg yr^{-1} from being emitted in 2050 compared to the business-as-usual scenario, a flux greater than Brazil's current primary anthropogenic Hg emissions[3]. A potential global reforestation scenario would reduce Hg inputs to the ocean by 98 Mg yr^{-1}, nearly 5% of global anthropogenic emissions. This study shows that land use change should be considered in anthropogenic Hg emissions inventories and illustrates potential benefits of land use policy to address global Hg pollution.

Introduction

Humans are exposed to the organic form of mercury (Hg), methylmercury (MeHg) through fish and seafood consumption[2]. Methylmercury is a potent neurotoxin, impairing the neurodevelopment of fetuses and children and costing the global economy $20–117 billion annually according to some estimates[14,15]. Mercury is emitted to the atmosphere by 1) primary anthropogenic sources, including artisanal and small-scale gold mining (ASGM), fossil fuel combustion, and metal smelting; 2) re-emissions of historical anthropogenic ("legacy") Hg from ocean and land; and 3) geogenic sources[16]. Mercury is globally dispersed in the atmosphere due to its long lifetime of 4–6 months[17]. A global treaty, the Minamata Convention on Mercury, aims to protect human health and the environment from anthropogenic emissions and releases of Hg. Its measures target primary anthropogenic emissions sources by phasing out Hg use and adopting best available technologies for pollution control[12]. However, primary anthropogenic emissions account for only 30% of present-day total emissions, with legacy re-emissions from land and ocean accounting for 60%[18]. The future of Hg pollution will depend not only on reducing direct emissions through the Minamata Convention, but also on indirect anthropogenic influences on legacy Hg emissions and fate.

Terrestrial ecosystems, and especially forests, are important sinks of Hg from the atmosphere, taking up an estimated 2200–3600 Mg Hg per year[4], more than a third of total (anthropogenic, legacy, and geogenic) Hg emissions (7400 Mg yr^{-1})[3]. By taking up Hg, terrestrial ecosystems reduce the burden of Hg depositing in oceans, where it can be converted to MeHg and bioaccumulated in fish. Previous studies have drawn useful analogies between Hg and carbon cycling in terrestrial ecosystems[19,20]. Like carbon dioxide (CO_2), elemental mercury (Hg^0) is assimilated by foliage throughout the growing season[21]. Mercury is transported from the canopy to soil through foliage falling to the ground ("litterfall") and being washed off by precipitation ("throughfall"), which together are the major source (60–90%) of Hg in soils[4]. Land cover changes (e.g., deforestation) perturb both CO_2 and Hg fluxes to the atmosphere[8,22,23]. In the case of carbon, scientific assessments have calculated the contribution of land use change to total CO_2 emissions (13% of total[22]), and land management practices are governed by Article 5 of the Paris Agreement[24]. For Hg, on the other hand, quantitative information related to the overall importance of land use change is limited. No anthropogenic emissions inventories consider the impacts of historical and future land use change, and land use change is not currently addressed by Hg policy efforts like the Minamata Convention.

The Amazon, as the largest tropical forest on the planet, has long been acknowledged as an important terrestrial carbon reservoir[25]. In parallel, studies have emerged highlighting the

Amazon's role as a sink for atmospheric Hg pollution[4,8,26], with the Amazon contributing an estimated 29% to the total Hg^0 land sink[7]. However, the future of the Amazon carbon and Hg sink is threatened by deforestation, mainly due to agricultural land conversion[13,25]. If deforestation continues at its current rate, 40% of the forest could be lost by 2050[13]. Along with removing a strong atmospheric sink of Hg[8], deforestation also enhances the emissions of legacy Hg into the atmosphere. In the Amazon, deforestation occurs through *slash-and-burn* practices that emit Hg from forest and soil biomass during fires[27]. Removal of canopy shading leads to more insolation reaching soil, increasing photo-reduction and volatilization rates of Hg from soils[10]. Additionally, soils in deforested areas are subject to accelerated erosion rates, enhancing Hg export to downstream ecosystems[9,28,29].

Although socioeconomic drivers are currently causing deforestation in the Amazon region, ecosystem restoration (including reforestation) has been proposed as a potential measure to protect biodiversity and enhance the CO_2 sink[30]. Reforestation and afforestation are being studied as part of the solution to reach net zero greenhouse gas emissions in the future[31], though the efficacy of these measures has been debated[32,33]. The potential climate mitigation benefits of forestation would also not be realized without accompanying aggressive CO_2 emissions reductions[30,32]. The effects of forestation on the atmosphere-terrestrial exchange of Hg, and potential benefits for Hg sequestration on land, remain unquantified.

Here, we combine atmospheric (GEOS-Chem) and soil erosion (GloSEM) modelling to illustrate the impacts of land use changes on the global Hg cycle. First, we analyze the impact of future Amazon deforestation policy scenarios[13] on the mass balance of Hg in soils, quantifying an overall 65% reduction in the Amazon Hg sink from 2003 to 2050 forest cover under a business-as-usual scenario. Second, we model the enhancement of the terrestrial Hg sink (+98 Mg yr^{-1}) under proposed global reforestation efforts. The magnitude of land use change impacts in the studied scenarios (~100 Mg yr^{-1}) is similar in magnitude to the primary anthropogenic emissions from the 4th highest Hg-emitting country in 2015 (Peru; 122 Mg yr^{-1})[3], highlighting the importance of conservation and restoration policies for curbing Hg pollution.

Results and discussion

Deforestation endangers the Amazon Hg sink

Using the global atmospheric Hg model GEOS-Chem[7], we investigate the impact of projected Amazon deforestation on the surface-atmosphere exchange of Hg. We ran simulations keeping anthropogenic Hg emissions constant at 2015 levels and evaluated Hg cycle changes due to variations in forest coverage. Under the historical forest coverage from 2003 (HIST

simulation), the Amazon rainforest stands out as a strong regional sink of Hg (Figure 1a), with net input from the atmosphere to the rainforest totalling 332 Mg yr^{-1}. We apply two deforestation scenarios for 2050 developed for the Amazon region[13]: a business-as-usual scenario (BAU), which extrapolates historical deforestation tendencies into the future, and a governance scenario (GOV), which assumes expanded conservation of the rainforest in the future. In the BAU scenario, widespread deforestation, mainly in eastern Amazonia, reduces the net Hg inputs to soils (Figure 1b). The removed vegetation leads to decreased Hg^0 deposition in the Amazon (change from HIST: -105 Mg yr^{-1}), enhanced Hg^0 emissions from soils newly exposed to light (+35 Mg yr^{-1}), and biomass burning emissions (+15 Mg yr^{-1}). The BAU scenario shows atmospheric Hg^0 concentrations increasing up to 0.3 ng m^{-3} within the Amazon region (Supplementary Figure S7); this would be a detectable change in Hg^0, comparable to the 0.5 ng m^{-3} decrease between 1995–2015 in North American Hg^0 observations[34]. In the GOV scenario, deforestation is slowed by the conservation measures, leading to smaller perturbations in the dry deposition flux (-47 Mg yr^{-1}) and the soil emission flux (+16 Mg yr^{-1}) (Figure 1b). Globally, the weakened rainforest sink of Hg yields higher deposition of Hg to oceans compared to the reference simulation (BAU – HIST = +108 Mg yr^{-1}; GOV – HIST = +44 Mg yr^{-1}).

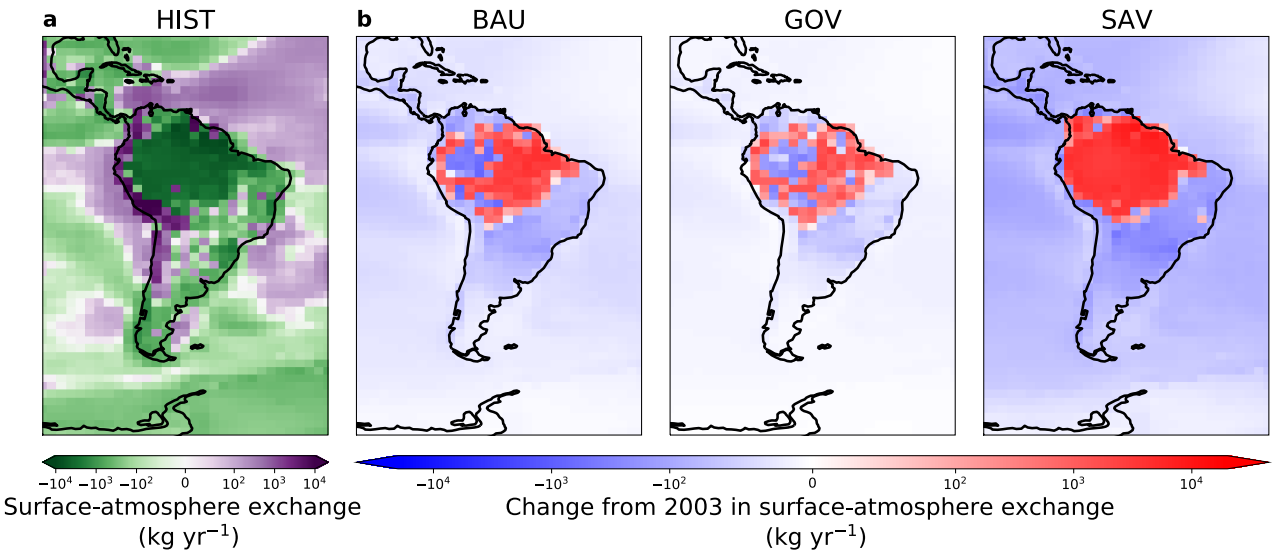

Figure 1. Impacts of Amazon deforestation on surface-atmosphere Hg exchange. a. The simulated surface-atmosphere exchange (net deposition is negative and net emission is positive) of Hg in the reference simulation (HIST). **b.** Changes in the exchange fluxes from the reference year are shown for the different deforestation scenarios: Business-as-usual (BAU), Governance (GOV), and complete Savannization (SAV); compared to the reference simulation, negative values refer to increased net fluxes to the surface and positive values refer to increased net fluxes to the atmosphere.

This change in the fate of atmospheric Hg (deposition to ocean instead of land) affects both the distribution and bioavailability of Hg. When sequestered in soils, Hg has an estimated residence time on the order of hundreds of years, whereas in the surface ocean Hg is recycled to the atmosphere within months to years[18,20]. Deforestation thus increases the mobility of Hg by transferring Hg from locally-sequestered reservoirs to the global pool. Human health risks are driven by exposure to the more toxic form of the element, MeHg, which is produced through methylation in the environment[1,14]. Deforestation shifts Hg inputs from land to the ocean, where Hg can more readily be methylated and bioaccumulate to dangerous levels in commercial fish. Methylation and bioaccumulation of Hg can also occur in forested soils, but MeHg levels in aquatic ecosystems are generally much higher (overall global ocean average = 15%)[35] than in Amazonian soils (1–5%)[26,36] . In addition, the long length of aquatic food chains leads to high levels of MeHg in commonly consumed fish species at higher trophic levels (e.g., tuna, cod, and swordfish)[1].

The consequences of deforestation on Hg pollution in the Amazon occur over multiple spatial scales, which we can explore with the atmospheric and soil erosion models. Soil erosion calculations are conducted with a semiempirical modelling approach, GloSEM (Global Soil Erosion Modelling)[29]. The total flux of eroded Hg from Amazon soils to riverine systems increases to 85 Mg yr^{-1} under BAU deforestation, compared to 64 Mg yr^{-1} in HIST and 73 Mg yr^{-1} in GOV. On top of being impacted by the increased transfer of Hg from soils to rivers, nearby ecosystems downstream of deforestation often show enhanced Hg methylation activity due to deforestation increasing organic carbon inputs and favouring anoxic conditions[37]. Mercury pollution in distant forested areas in the Amazon can worsen through long-range atmospheric Hg transport and deposition because of the removed sink capacity after deforestation. Remaining forested areas in western Amazonia experience enhanced Hg^0 dry deposition (up to +20% in BAU) after deforestation occurs elsewhere (Figure 1b). The increased Hg inputs to remaining forests are driven by higher atmospheric Hg^0 concentrations after deforestation (Supplementary Figure S7a).

Deforestation can be exacerbated through climate feedbacks, which are not considered in these policy scenarios. For example, BAU projects that 40% of the Amazon will be deforested by 2050[13], which could trigger a tipping point with widespread transition of the rainforest to a savannah biome under diminished regional moisture recycling[38]. To evaluate this, we also ran an upper limit scenario[7,39] where the entire rainforest is converted to savannah (SAV). In this case, ocean inputs of Hg increase by 343 Mg yr^{-1}, driven by both decreased Hg^0 dry deposition (-359 Mg yr^{-1}) and increased Hg^0 soil emissions (+89 Mg yr^{-1})

in the Amazon region (Figure 1b). The perturbation to ocean Hg inputs is larger than the value (283 Mg yr^{-1}) predicted by our previous work[7], which did not account for the soil Hg^0 emission feedback.

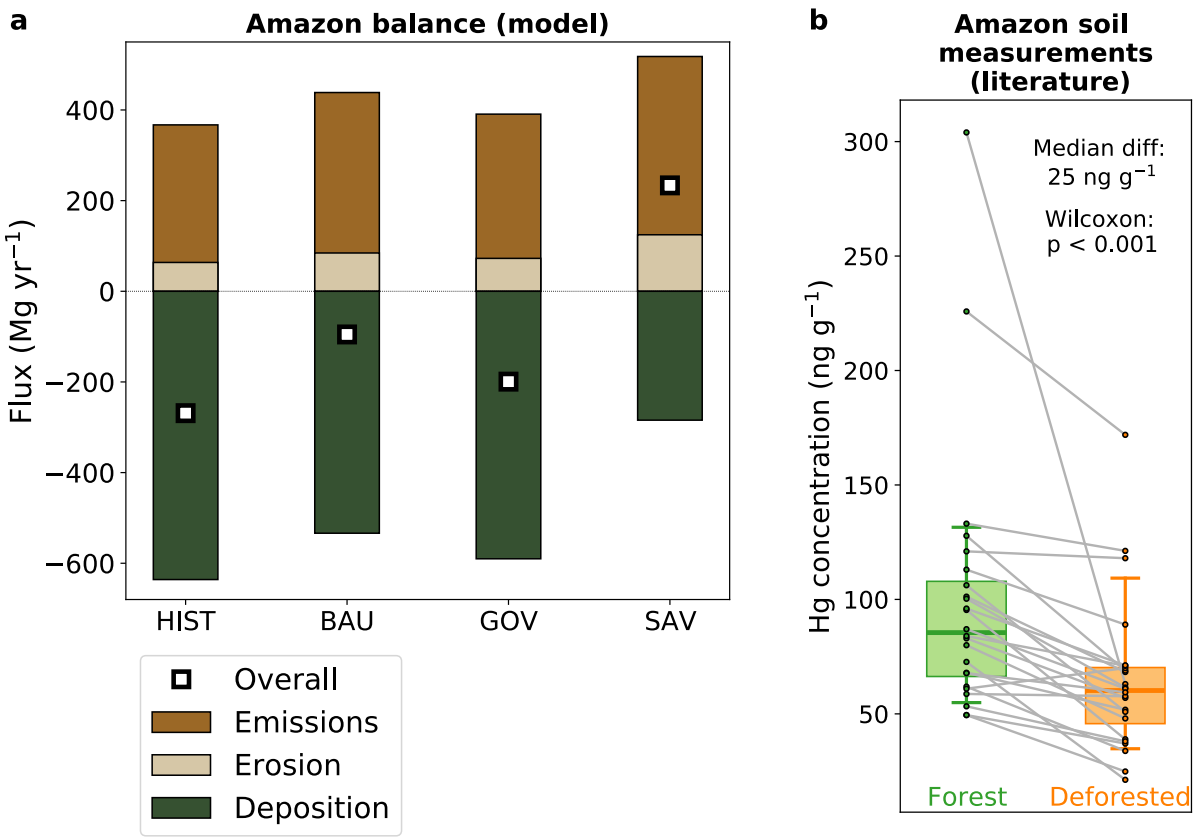

Figure 2. The mass balance of Hg in the Amazon. a. Total simulated fluxes of Hg emissions, erosion, and deposition are calculated for the Amazon region in each scenario. White squares illustrate the overall mass balance of Hg for the land surface (= emissions – deposition – erosion). **b.** Measured Hg concentrations in forest (green) and deforested (orange) soils (0–20 cm depth) from the literature (n = 24; for references see Supplementary Information Spreadsheet). Box plots show the median values (solid lines), interquartile range (shaded), and 10th and 90th percentiles (whiskers). Gray lines connect paired sites from the same study. Listed p-value (<0.001) refers to the Wilcoxon signed-rank test of the null hypothesis that paired forest and deforested sites come from the same distribution.

Land use change substantially impacts the mass balance of Hg in the Amazon region, by altering both atmosphere-terrestrial exchange and erosion (Figure 2a). In HIST, the Amazon is a strong terrestrial sink of Hg (269 Mg yr^{-1}). If agricultural expansion continues as in BAU, the net Amazon Hg sink is weakened by 65% to 95 Mg yr^{-1}. Under the more moderate GOV scenario, the Amazon Hg sink (199 Mg yr^{-1}) is better preserved, though still 26% smaller than HIST. Stricter conservation policies in GOV yield an additional 104 Mg yr^{-1} of Hg sequestered in the Amazon compared to BAU. The majority of the mass balance perturbation is driven by changes to the atmosphere-terrestrial exchange; nevertheless,

deforestation also enhances Hg erosion in both scenarios (BAU: +33%; GOV: +14%), accelerating the transfer of terrestrial Hg to aquatic ecosystems. The SAV scenario illustrates that additional climate feedbacks can flip the Amazon from a net Hg sink to a source (+234 Mg yr^{-1}). These Hg projections parallel recent findings on Amazon carbon cycling, which have demonstrated that climate change and deforestation are turning the Amazon into a CO_2 source[25].

To assess whether projected Hg fluxes driven by deforestation are compatible with available field observations, we compiled a literature database of studies that compared Hg concentrations in deforested Amazonian soils with nearby forest plots (Supplementary Information Spreadsheet). In the surface layer of soils (0–20 cm), forested areas show higher Hg concentrations (median: 86 ng g^{-1}; 10th–90th percentile (P10–P90): 51–179 ng g^{-1}) than deforested areas (median: 60 ng g^{-1}; P10–P90: 29–120 ng g^{-1}) (Figure 2b). Deforested sites show a consistent decrease compared to paired forested sites (p-value < 0.001; Wilcoxon signed-rank test), with the median decrease being 25 ng g^{-1} (P10–P90: 2–58 ng g^{-1}). We scale the median decrease from these studies to the SAV scenario, where the entire Amazon forested area (5.3 million km^2; ref[13]) is removed, assuming average Amazon soil density of 1.25 ng g^{-1} and that deforested soils in the literature studies were measured 10 years after deforestation. The Hg loss for the uppermost 10 cm of soil scales to 1683 Mg yr^{-1} (P10–P90: 132–3823 Mg yr^{-1}) if the entire Amazon is deforested. This literature-based range can be compared to the modelled difference (503 Mg yr^{-1}) between the Amazon Hg mass balance in SAV (+234 Mg yr^{-1}) and HIST (-269 Mg yr^{-1}). The modelled impact of deforestation (503 Mg yr^{-1}) is compatible with the literature-based estimated range (132–3823 Mg yr^{-1}). Despite the limited number of sites (n = 24 pairs) in this back-of-the-envelope calculation, available literature studies support the modelling conclusions that substantial amounts of Hg are mobilized from the terrestrial biosphere by deforestation.

Impact of reforestation on Hg fluxes

Reforestation has been identified as a potential mitigation approach for climate change, by strengthening the terrestrial CO_2 sink[30,40]. To investigate potential impacts on Hg cycling, we investigated a global reforestation scenario (RFR) based on the Global Reforestation Potential Map[30,41], which identified areas suitable for reforestation worldwide (i.e., not including croplands or areas where forests are not native). Figure 3a maps the impacts of reforestation on Hg surface-atmosphere exchange, comparing to the reference HIST simulation. Globally, RFR enhances uptake of Hg on land by 98 Mg yr^{-1}, similarly reducing Hg deposition to

oceans. Reforestation could thus take up approximately 5% of the anthropogenic Hg emission flux (~2000 Mg yr^{-1})[3]. In addition to the targeted benefits for biodiversity and climate change mitigation[30], reforestation could moderately reduce levels of Hg in marine ecosystems, and hence commercial fish. Nevertheless, the magnitude of reforestation impact (5% of primary emissions) illustrates that reforestation is not a substitute for implementing extensive cuts to primary Hg emissions, like in the CO_2 context[32].

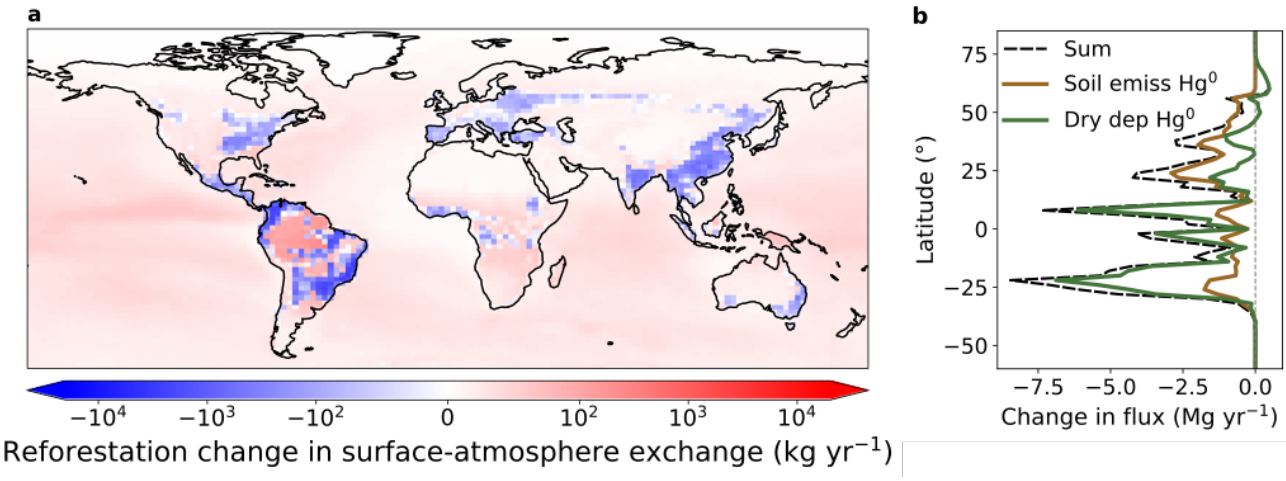

Figure 3. Enhanced land sink of Hg with reforestation. a. The impact of RFR scenario on surface-atmosphere exchange. The differences from the reference HIST simulation are shown, with negative values referring to increased net fluxes to the surface and positive values referring to increased net fluxes to the atmosphere. **b.** Zonal (latitudinal) changes to Hg land sink fluxes driven by reforestation. Changes in soil emissions of Hg^0 and dry deposition of Hg^0 to land (RFR – HIST) are plotted (negative values refer to increased net fluxes to the surface; thus, both increased dry deposition and decreased soil emissions are displayed as negative).

Potential reforestation opportunities for Hg are dominated by the Amazon and Atlantic forest regions in South America (71 Mg yr^{-1}, 72% of total land sink impact) (Figure 3b). The land sink impact is driven by the combination of increased Hg^0 dry deposition fluxes to vegetation and decreased Hg^0 soil emissions due to new forest areas, although the importance of these two processes varies by latitude (Figure 3b). In the tropics and Southern Hemisphere (south of 15°N), increases in Hg^0 dry deposition contribute to 75% of the enhancements in the Hg land sink, while decreases in soil emissions of Hg^0 contribute 25%. In contrast, for latitudes north of 15°N, reductions in soil emissions are more important (78% contribution) than increases in dry deposition (22%) in driving the enhanced land sink (Figure 3b). The zonal drivers of the land sink can be explained by Hg-contaminated soils being more prevalent in the Northern extratropics, impacted by higher historic anthropogenic Hg emissions[42]. On the other hand, productive tropical and subtropical forests generally take up

more Hg^0 than forests in the Northern extratropics[43], resulting in a stronger response in Hg^0 dry deposition for these latitudes. Given the zonal distribution of reforestation impacts on the atmosphere-terrestrial exchange of Hg (Figure 3), it is clear that reforestation efforts in Northern extratropical areas alone (-29 Mg yr^{-1}) cannot compensate for deforestation Hg emissions in the Amazon (BAU: +153 Mg yr^{-1}; GOV: +61 Mg yr^{-1}). Overall, more information would be needed to compare the global magnitude of Hg sequestered by reforestation compared to conservation policies, as the deforestation scenarios focused only on a specific region (the Amazon), neglecting conservation impacts in other tropical regions (e.g., in Africa and Southeast Asia).

Land use change fluxes are on par with country-level emissions

Atmospheric Hg fluxes from deforestation and reforestation are substantial when compared to country-level 2015 anthropogenic Hg emissions[3]. For example, Amazon deforestation in the BAU case yields a net release of 153 Mg yr^{-1} to the atmosphere relative to HIST, which, if considered among current country-level emissions, would be the 4th largest anthropogenic emitter behind China, India, and Indonesia (Figure 4). Climate change can exacerbate Amazon land use emissions further, with the extreme SAV simulation showing 441 Mg yr^{-1} additional emissions, behind only China's anthropogenic Hg emissions. Amazon conservation (GOV vs. BAU) removes 92 Mg yr^{-1} from the atmosphere, immobilizing a flux on par with primary anthropogenic Hg emissions from countries in the region like Brazil (71 Mg yr^{-1}) and Peru (122 Mg yr^{-1}). Likewise, the global reforestation scenario (RFR) would have a similar atmospheric impact (-98 Mg yr^{-1} compared to HIST) as Amazon conservation. The relative importance of land use change as an anthropogenic driver of Hg pollution could increase over time, with primary anthropogenic emissions of Hg projected to halve to 1020 Mg yr^{-1} by 2035 under Minamata policies and reductions in fossil fuel use[44]. Therefore, there is an urgent need to accurately account for land use change emissions in Hg assessments. More aggressive reductions to primary anthropogenic Hg emissions may also be required to compensate for these previously uncounted land use change emissions.

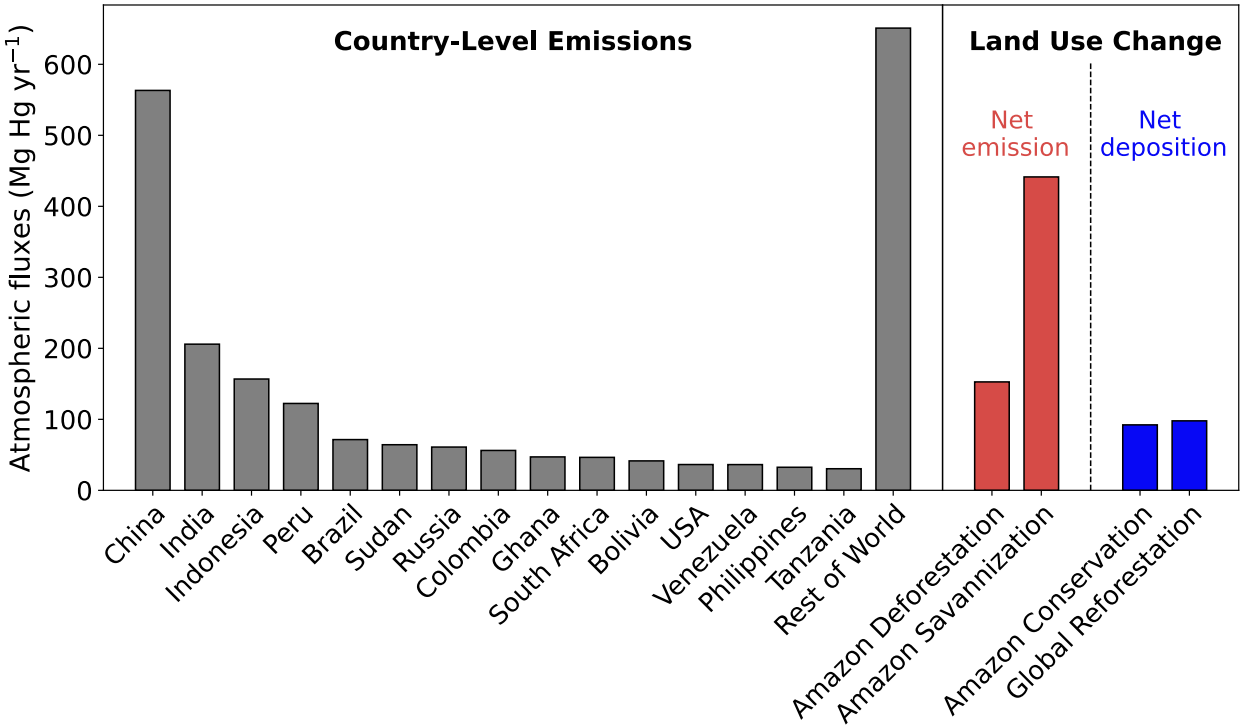

Figure 4. Substantial impact of land use change on atmospheric Hg fluxes. Land use change net atmospheric fluxes computed in this study are compared to country-level primary Hg emissions in 2015 (gray), according to the Global Mercury Assessment inventory from AMAP/UNEP[3,45]. For land use change fluxes, net atmospheric emission fluxes are shown in red and net atmospheric deposition fluxes are blue. Listed land use change fluxes: Amazon Deforestation — comparing Amazon land sink in BAU vs. HIST; Amazon Savannization — comparing Amazon land sink in SAV vs. HIST; Amazon Conservation — comparing Amazon land sink in GOV vs. BAU; Global Reforestation — comparing global land sink in RFR vs. HIST.

Implications for global Hg inventories and policy

The 2021 Glasgow Declaration, endorsed by 145 countries, committed to stopping and reversing deforestation by 2030 to promote sustainable land use and fight climate change[46]. As shown by our current work, significant amounts of legacy Hg can be sequestered or released by land depending on the success or failure of these efforts. Until now, scientific assessments[3] have focused on quantifying primary anthropogenic Hg emissions, and specific measures in the Minamata Convention[12] address primary Hg emissions. One clear path forward for scientific assessments would be to develop global inventories and projections for land use change emissions of Hg, as has been done for greenhouse gases[22]. Land use driven fluxes in Hg (here calculated as ~100 Mg yr^{-1}) are considerable compared to the estimated changes in primary anthropogenic emissions between 2000 and 2015 (~400 Mg yr^{-1}; ref[47]). Therefore, inclusion of land use emissions in assessments is important for accurately representing the drivers of Hg trends. Future Hg emissions scenarios also do not yet consider land use changes[44], which could distort predictions of future Hg deposition and health

impacts. Land use emission inventories would provide a more comprehensive picture of the anthropogenic impact on the Hg cycle, enabling potential collaborations to emerge between the Minamata Convention and other global policy efforts to reduce deforestation.

Enhanced Hg immobilization on land represents a heretofore unquantified co-benefit of reforestation and forest conservation. New forest cover will increase Hg levels in soils, with retention depending on local environmental and geochemical factors such as minerology[48,49] and the amount of soil organic carbon[6]. Similar to CO_2, the efficacy of reforestation for Hg mitigation depends on whether the storage of Hg in soils is over a long-term period. Potential benefits of enhanced Hg and CO_2 uptake on land can be reversed by human or natural disturbances, e.g., climate change increasing the frequency of wildfires — which re-emit Hg and carbon from terrestrial ecosystems — and droughts — which reduce Hg and CO_2 uptake by plants[30,50]. Thus, mitigation of Hg pollution by conserving and increasing forest area can only be realized with concurrent efforts to sustainably manage land areas and preventing severe climate change.

Here, we have quantified the significant impact that anthropogenic activities have on atmospheric fluxes and erosion of Hg through land cover change. However, many more global change drivers (e.g., climate change, forest harvest, agricultural practices) can perturb the terrestrial storage of Hg. Further development of Hg cycles and driving processes within Earth system models will be vital to investigate the evolution of the Hg land sink over time and the effect on environmental Hg risks. Ultimately, mitigation of global Hg pollution depends not only on reducing primary anthropogenic emissions, but also reducing anthropogenic activities like deforestation that re-mobilize legacy Hg.

Methods

Atmospheric Hg model (GEOS-CHEM) description

In this study, we use GEOS-Chem v12.8.1 with Hg^0 dry deposition updates from Feinberg et al.[7]. The global model is run at 2.0° × 2.5° horizontal resolution and 47 vertical layers up to 80 km altitude. The model tracks emissions, transport, chemistry, and deposition of Hg in three chemical tracers: elemental mercury (Hg^0), oxidized mercury (Hg^{II}), and particulate-bound mercury (Hg^P). Atmospheric transport of Hg species is based on MERRA-2 reanalysis meteorological data[51]. The Hg chemical mechanism assumes that Br is the primary Hg oxidant and uses offline monthly maps of previously-calculated oxidant concentrations to drive chemistry[52,53]. The aqueous photoreduction rate of Hg^{II} to Hg^0 is parametrized as depending on the organic aerosol concentration and the NO_2 photolysis rate[52].

The wet removal of oxidized Hg (Hg^{II} and Hg^{P}) from the atmosphere is calculated in online parametrizations considering large-scale and convective scavenging of gas and particulate species[54,55]. Dry deposition in GEOS-Chem is calculated using a resistance-based approach[56,57], which determines the dry deposition velocities depending on meteorology (e.g., temperature and windspeed), land surface parameters (e.g., land type and leaf area index, LAI), and compound-specific parameters (biological reactivity, f_0, and solubility, H^*). For Hg^0, f_0 is set to 0.2 within the Amazon rainforest and 3×10^{-5} elsewhere, which was found to yield the best agreement with measurements of Hg^0 vegetation uptake[7]. The solubility of Hg^0 is low ($H^* = 0.11$ M atm^{-1})[58], whereas gaseous Hg^{II} is assumed to be highly soluble ($H^* = 10^{14}$ M atm^{-1}) and biologically unreactive ($f_0 = 0$). Dry deposition of Hg^P is determined according to the standard aerosol deposition parameterization in GEOS-Chem[59,60]. Dry deposition is calculated separately over each land type within a grid cell (e.g., rainforest, grassland, cropland, etc.) and then an overall area-weighted average is calculated for the grid cell. GEOS-Chem accounts for 73 land types based on the Gibbs[61] land cover product. The LAI data for this study is taken from a reprocessed version of the Moderate Resolution Imaging Spectroradiometer (MODIS) satellite product[62]. Dry deposition of Hg^0 over the ocean is not calculated within the resistance-based scheme, as it is instead accounted for in the air-sea exchange parametrization[63].

Anthropogenic Hg emissions follow AMAP/UNEP estimates[45] for 2015. Biomass burning emissions are taken from the Global Fire Emissions Database (GFED) v4.1s (ref[64]). Emissions of Hg^0 from snow and geogenic sources, as well as prompt recycling of 20% of recently deposited Hg^{2+} to land, follow Selin et al.[65]. We use fixed concentrations of Hg^0 in the surface ocean based on the MITgcm 3-D ocean model[52] to calculate the Hg^0 air-sea exchange[63]. We adopted a new formulation[66] for the soil Hg^0 emissions parametrization (Supplementary Information, Section S2):

$$E_{\text{soil}} = aC^b R_g^c \qquad (1)$$

where E_{soil} is the Hg^0 emissions from soil (units ng m^{-2} h^{-1}), C is the concentration of Hg in soils, R_g is solar radiation flux at the ground, and a, b, and c, are coefficients (set to 71, 2.5, and 0.76, respectively). We have tuned the coefficients of this parametrization to match available soil emissions measurements from the Amazon and extratropics (Supplementary Information, Section S2). The soil concentration map of Hg (C) was calculated using the method of Selin et al.[65], deriving the spatial distribution of soil concentrations by first assuming a steady state balance between land emissions and deposition in the preindustrial and subsequently increasing soil concentrations according to the distribution of anthropogenic

Hg deposition. As in Selin et al.[65], the solar radiation at ground (R_g) is determined by considering attenuation of the solar radiation flux (R_S) by shading from the overhead canopy, parametrized by the LAI:

$$R_g = R_S \exp\left(-\frac{\alpha \mathrm{LAI}}{\cos\theta}\right) \qquad (2)$$

where $\alpha = 0.5$, assuming extinction from a random angular distribution of leaves[67] and θ is the solar zenith angle. We have also updated GEOS-Chem to calculate soil emissions at the sub-grid scale for each land use category contained within the grid cell.

Erosion model (GloSEM) description

The annual potential rates of soil displacement by water erosion (soil erosion) for the deforestation scenarios are estimated using the RUSLE-based[68] modeling platform Global Soil Erosion Modeling (GloSEM)[29,69]. As a detachment-limited soil erosion prediction model, GloSEM estimates soil erosion (expressed as a mass of soil lost per unit area and time, Mg ha^{-1} yr^{-1}) due to inter-rill and rill erosion processes by multiplication of six contributing factors. The modelling scheme follows the same principle of most RUSLE-type models or more complex catchment-scale process-based models, with a driving force (erosivity of the climate), a resistance term (erodibility of the soil) and other factors representing the farming choice, i.e., topographical conformation of the field, cropping system, and soil conservation practices.

Our approach for calculating soil erosion in the Amazon scenarios is similar to the GloSEM parametrization adopted by Borrelli et al.[29,69] to estimate human-induced soil erosion change between 2001 and 2070 at a global scale. The horizontal resolution of the native soil erosion modelling is 250 × 250 m. For this study, we adapted the computation of the land cover and management factor (C-factor), which measures the combined effect of vegetation cover and cropping system variables on the soil erosion process. We parametrize the C-factor according to two layers of information: 1) the spatial dimension of land use classes according to the deforestation scenarios from Soares-Filho et al.[13] (described below); 2) the vegetation condition in each land use class using the MODIS MOD44B Vegetation Continuous Fields product (VCF) (~250m spatial resolution) as a proxy to quantify (i) surface vegetation cover, (ii) tree cover, and (iii) bare soil. The full calculation of the C-Factor is detailed in the Supplementary Information (Section S5).

Following Lugato et al.[70] we assume that 30% of the eroded soil flux is not redeposited on land and enters riverine systems. We calculate the eroded flux of Hg from land

by multiplying the soil flux by the median Hg concentration in Amazon forested soils from a literature review (86 ng g^{-1}; see SI Spreadsheet).

Model inputs for Amazon deforestation scenarios

We employ deforestation scenarios from Soares-Filho et al.[13], who developed a model for predicting the extent of deforestation within the Amazon based on environmental policies and highway construction. They presented two scenarios, encompassing a range of future deforestation trajectories: a Business as Usual (BAU) scenario and a Governance (GOV) scenario. In the BAU scenario, recent deforestation trends continue into the future, assuming that compliance with conservation laws remains low and no new areas will be protected. On the other hand, the GOV scenario assumes the expansion of environmental legislation and increased enforcement of protected areas will lead to a reduction in the deforestation rate. Compared to the Amazon forest area in 2003 (5.3 million km^2), in 2050 the BAU scenario projects 3.2 million km^2 remaining (-40% of 2003 area) and GOV projects 4.5 million km^2 remaining (-15%)[13]. These scenarios were published in 2006, after which the political and conservation landscape in the Amazon region has continued to evolve[71,72]. Nevertheless, the deforestation rates projected by these scenarios are similar to deforestation data observed by the Landsat satellite, with recent rates 2012–2019 falling closer to the BAU scenario (Supplementary Figure S2). We focus our analysis on comparing the forest coverage in the years 2003 and 2050, with these policy scenarios being the only available projections (to our knowledge) forecasting likely ranges of deforestation for 2050 in the entire Amazon basin.

We translated these scenarios into required inputs for the calculations in GEOS-Chem (spatially gridded land use categories, LAI, and biomass burning emissions) and GloSEM (spatially gridded land use categories and vegetation cover, see SI Section S5). We used year 2003 data as the base maps for LAI and biomass burning datasets, with the HIST simulation using these reference datasets. The Soares-Filho et al.[13] dataset assigns 1 km^2 pixels within the Amazon basin as being forested, deforested, or agricultural areas for every year between 2003 and 2050. We regridded these annual datasets to 0.25° × 0.25° resolution, the native resolution of land use and LAI maps in GEOS-Chem. We calculated the relative change in forested area in the scenarios for every 0.25° × 0.25° grid cell. The rainforest land use category in deforested grid cells is correspondingly reduced by this factor, with the lost land area added to the land use category for “Fields and Woody Savanna”. The LAI annual cycle for existing Fields and Woody Savanna grid cells within the Amazon basin was spatially averaged over 2003 and assigned to the deforested areas. Annual average LAI maps for the

Amazon scenarios used in GEOS-Chem are shown in Supplementary Figure S5. Gridded biomass burning emissions are calculated by multiplying the newly deforested areas for each year by mean fire Hg emissions (380 μg m^{-2} yr^{-1}) from two observational studies in the Amazon[27,73]. An additional 50% of the emissions (190 μg m^{-2} yr^{-1}) are released to the atmosphere within the first year as post-burn Hg^0 emissions from soils[10]. To account for seasonal differences in meteorology and realistic timing for forest clearing and burning, we assumed that deforestation occurs at the start of June and deforestation biomass burning emissions occur in August and September[73].

The BAU and GOV scenarios do not account for any land-climate feedbacks[13], wherein deforestation of the rainforest can lead to reduced moisture recycling and widespread *savannization* (conversion of rainforest to savanna)[38,74]. As an upper bound for this process, we consider an extreme scenario (SAV) where the Amazon rainforest is fully converted to savanna[39]. The impact of this scenario on Hg^0 deposition was previously quantified[7], but here we reran the SAV simulation in GEOS-Chem to account for updates in the soil Hg^0 emissions parametrization.

Model inputs for potential reforestation scenario

We apply a reforestation scenario (RFR) in GEOS-Chem based on the Global Reforestation Potential map[30,41], which considers the binary potential of every 1 km^2 grid cell to be converted from non-forest (<25% tree cover in 2000–2009) to forest (>25% tree cover). The reforestation potential dataset does not include areas that are native non-forest land cover types (e.g., grasslands) or cropland areas. We regridded the reforestation potential to 0.25° × 0.25° resolution, calculating the area fraction suitable for reforestation at the model's input grid resolution. For every grid cell where reforestation can occur, we identify the corresponding biome in the Ecoregions2017 dataset[75] to determine the type of native forest vegetation that would occur. If the corresponding biome of the grid cell is not a forest (e.g., in cases where the coarse coastal grid cell of the model is assigned to water in the Ecoregions2017 dataset), we identify the most common forest type in the 8 neighbouring grid cells. The added forest is assumed to have a LAI annual cycle equal to the 2003 spatial average for all grid cells in the corresponding biome and biogeographic realm (LAI_{biome}). For grid cells that are not a forest land type in 2003, we subtract the reforested area fraction (f_{rfr}) from the original land type and add the reforested area fraction to the new forest land type. We only reforest grid cells in the case where LAI_{biome} is larger than the original land type LAI (LAI_{old}). Since the land map used in GEOS-Chem is at coarser resolution (0.25° × 0.25°) than

the reforestation potential dataset (1 km × 1 km), the reforested grid cell may already be a forest land type in GEOS-Chem. In this case, we assume that the grid cell LAI (LAI_{new}) will become denser due to the new reforested area:

$$\mathrm{LAI_{new}} = \mathrm{LAI_{old}} + f_{\mathrm{rfr}} \cdot \mathrm{LAI_{biome}} \quad (3)$$

The resultant average LAI map in the RFR scenario is shown in Supplementary Figure S6.

GEOS-Chem simulations

We run GEOS-Chem simulations for the land cover conditions of 2003 (HIST simulation), 2050 in the BAU scenario, 2050 in the GOV scenario, the SAV scenario, and the RFR scenario. To highlight the role of land cover changes alone, we keep meteorological conditions constant by running the simulations with meteorology for 2014–2015. We consider the first year as spinup to equilibrate the new land cover conditions, and analyze simulation differences for the meteorological year 2015.

To calculate the Amazon terrestrial Hg mass balance, we combine the GloSEM erosion model results with GEOS-Chem outputs. We defined the Amazon region based on the area covered by the Soares-Filho et al.[13] deforestation projections (shown in Supplementary Figure S1). Within the Amazon region, we calculate the Hg mass balance (B) by summing the fluxes exported from the region (emissions and erosion) and subtracting fluxes into the region (deposition):

$$B = F_{\mathrm{erosion}} + E_{\mathrm{soil}} + E_{\mathrm{BB}} + E_{\mathrm{other}} - D_{\mathrm{dry}} - D_{\mathrm{wet}} \quad (4)$$

where F_{erosion} is the erosion flux, E_{soil} are the emissions of Hg^0 from soil, E_{BB} are the emissions of Hg^0 due to biomass burning during deforestation, and E_{other} are all other Hg emissions that do not change between simulations (including from ASGM, geogenic sources, and wildfires). Deposition occurs both through dry deposition (D_{dry}) and wet deposition (D_{wet}). We consider the overall balance of all Hg species, i.e., Hg^0, Hg^{2+}, and Hg^P.

Acknowledgements

This work was funded by the Swiss National Science Foundation through an Early Postdoc.Mobility grant to A.F. (P2EZP2_195424) and an Ambizione grant to M.J. (PZ00P2_174101), a grant (#1924148) from the US National Science Foundation to N.E.S., and an Academic Transition Grant from Eawag to J.B. We thank Ronny Meier and Michael Windisch for assistance in processing the reforestation potential dataset. We thank Luiz D. Lacerda for sharing Hg data from Brazil. We acknowledge researchers involved in conducting

field studies measuring the impact of deforestation on Hg fluxes in the Amazon and elsewhere.

Author contributions

All authors conceived the study. M.J., J.B., and A.F. compiled Hg field data through literature review. A.F. and P.B performed the simulations. All authors contributed to the data analysis. A.F. wrote the draft of the paper with contributions and revisions from all authors.

Data availability

Simulation data supporting the results of this study are published in Zenodo (https://doi.org/10.5281/zenodo.7566032) under a CC BY 4.0 license (https://creativecommons.org/licenses/by/4.0/).

Code availability

Model and analysis codes involved in producing the results of this study are published in Zenodo (https://doi.org/10.5281/zenodo.7566032).

References

1. Schartup, A. T. *et al.* Climate change and overfishing increase neurotoxicant in marine predators. *Nature* **572**, 648–650 (2019).
2. Sheehan, M. C. *et al.* Global methylmercury exposure from seafood consumption and risk of developmental neurotoxicity: a systematic review. *Bull. World Health Organ.* **92**, 254-269F (2014).
3. UNEP. *Global Mercury Assessment 2018*. (UN Environment Programme, Chemicals and Health Branch. Geneva, Switzerland, 2019).
4. Zhou, J., Obrist, D., Dastoor, A., Jiskra, M. & Ryjkov, A. Vegetation uptake of mercury and impacts on global cycling. *Nat. Rev. Earth Environ.* **2**, 269–284 (2021).
5. Obrist, D. *et al.* Previously unaccounted atmospheric mercury deposition in a midlatitude deciduous forest. *Proc. Natl. Acad. Sci. U.S.A.* **118**, e2105477118 (2021).
6. Hararuk, O., Obrist, D. & Luo, Y. Modelling the sensitivity of soil mercury storage to climate-induced changes in soil carbon pools. *Biogeosciences* **10**, 2393–2407 (2013).
7. Feinberg, A., Dlamini, T., Jiskra, M., Shah, V. & Selin, N. E. Evaluating atmospheric mercury (Hg) uptake by vegetation in a chemistry-transport model. *Environ. Sci.: Processes Impacts* (2022) doi:10.1039/D2EM00032F.
8. Fostier, A. H., Melendez-Perez, J. J. & Richter, L. Litter mercury deposition in the Amazonian rainforest. *Environ. Pollut.* **206**, 605–610 (2015).
9. Roulet, M. *et al.* Effects of Recent Human Colonization on the Presence of Mercury in Amazonian Ecosystems. *Water Air Soil Pollut.* **112**, 297–313 (1999).
10. Carpi, A., Fostier, A. H., Orta, O. R., dos Santos, J. C. & Gittings, M. Gaseous mercury emissions from soil following forest loss and land use changes: Field experiments in the United States and Brazil. *Atmos. Environ.* **96**, 423–429 (2014).

11. Magarelli, G. & Fostier, A. Influence of deforestation on the mercury air/soil exchange in the Negro River Basin, Amazon. *Atmos. Environ.* **39**, 7518–7528 (2005).
12. UNTC. *Minamata Convention on Mercury*. (2013).
13. Soares-Filho, B. S. *et al.* Modelling conservation in the Amazon basin. *Nature* **440**, 520–523 (2006).
14. Zhang, Y. *et al.* Global health effects of future atmospheric mercury emissions. *Nat Commun* **12**, 3035 (2021).
15. Bellanger, M. *et al.* Economic benefits of methylmercury exposure control in Europe: Monetary value of neurotoxicity prevention. *Environ Health* **12**, 3 (2013).
16. Outridge, P. M., Mason, R. P., Wang, F., Guerrero, S. & Heimbürger-Boavida, L. E. Updated Global and Oceanic Mercury Budgets for the United Nations Global Mercury Assessment 2018. *Environ. Sci. Technol.* acs.est.8b01246 (2018) doi:10.1021/acs.est.8b01246.
17. Shah, V. *et al.* Improved Mechanistic Model of the Atmospheric Redox Chemistry of Mercury. *Environ. Sci. Technol.* **55**, 14445–14456 (2021).
18. Amos, H. M., Jacob, D. J., Streets, D. G. & Sunderland, E. M. Legacy impacts of all-time anthropogenic emissions on the global mercury cycle. *Global Biogeochem. Cycles* **27**, 410–421 (2013).
19. Schaefer, K. *et al.* Potential impacts of mercury released from thawing permafrost. *Nat Commun* **11**, 4650 (2020).
20. Smith-Downey, N. V., Sunderland, E. M. & Jacob, D. J. Anthropogenic impacts on global storage and emissions of mercury from terrestrial soils: Insights from a new global model. *J. Geophys. Res.* **115**, G03008 (2010).
21. Jiskra, M. *et al.* A vegetation control on seasonal variations in global atmospheric mercury concentrations. *Nature Geosci* **11**, 244–250 (2018).
22. IPCC. *Climate Change and Land: an IPCC special report on climate change, desertification, land degradation, sustainable land management, food security, and greenhouse gas fluxes in terrestrial ecosystems*. (2019).
23. Zhang, H., Holmes, C. D. & Wu, S. Impacts of changes in climate, land use and land cover on atmospheric mercury. *Atmos. Environ.* **141**, 230–244 (2016).
24. UNFCC. *The Paris Agreement*. (2015).
25. Gatti, L. V. *et al.* Amazonia as a carbon source linked to deforestation and climate change. *Nature* **595**, 388–393 (2021).
26. Gerson, J. R. *et al.* Amazon forests capture high levels of atmospheric mercury pollution from artisanal gold mining. *Nat Commun* **13**, 559 (2022).
27. Melendez-Perez, J. J. *et al.* Soil and biomass mercury emissions during a prescribed fire in the Amazonian rain forest. *Atmospheric Environment* **96**, 415–422 (2014).
28. Fostier, A. H. *et al.* Mercury fluxes in a natural forested Amazonian catchment (Serra do Navio, Amapá State, Brazil). *Sci. Total Environ.* **260**, 201–211 (2000).
29. Borrelli, P. *et al.* Land use and climate change impacts on global soil erosion by water (2015-2070). *Proc. Natl. Acad. Sci. U.S.A.* **117**, 21994–22001 (2020).
30. Griscom, B. W. *et al.* Natural climate solutions. *Proc. Natl. Acad. Sci. U.S.A.* **114**, 11645–11650 (2017).
31. IPCC. Summary for Policymakers. in *Climate Change 2022: Mitigation of Climate Change. Contribution of Working Group III to the Sixth Assessment Report of the Intergovernmental Panel on Climate Change* ([P.R. Shukla, J. Skea, R. Slade, A. Al Khourdajie, R. van Diemen, D. McCollum, M. Pathak, S. Some, P. Vyas, R. Fradera, M. Belkacemi, A. Hasija, G. Lisboa, S. Luz, J. Malley, (eds.)]. Cambridge University Press, Cambridge, UK and New York, NY, USA).
32. Holl, K. D. & Brancalion, P. H. S. Tree planting is not a simple solution. *Science* **368**, 580–581 (2020).

33. Portmann, R. *et al.* Global forestation and deforestation affect remote climate via adjusted atmosphere and ocean circulation. *Nat Commun* **13**, 5569 (2022).
34. Zhang, Y. *et al.* Observed decrease in atmospheric mercury explained by global decline in anthropogenic emissions. *Proc. Natl. Acad. Sci. U.S.A.* **113**, 526–531 (2016).
35. Zhang, Y., Soerensen, A. L., Schartup, A. T. & Sunderland, E. M. A Global Model for Methylmercury Formation and Uptake at the Base of Marine Food Webs. *Global Biogeochem. Cycles* **34**, (2020).
36. Roulet, M., Guimarães, J.R.D, & Lucotte, M. Methylmercury production and accumulation in sediments and soils of an amazonian floodplain – effect of seasonal inundation. *Water, Air, and Soil Pollution* **128**, 41–60 (2001).
37. Hsu-Kim, H. *et al.* Challenges and opportunities for managing aquatic mercury pollution in altered landscapes. *Ambio* **47**, 141–169 (2018).
38. Lovejoy, T. E. & Nobre, C. Amazon Tipping Point. *Sci. Adv.* **4**, eaat2340 (2018).
39. Alves de Oliveira, B. F., Bottino, M. J., Nobre, P. & Nobre, C. A. Deforestation and climate change are projected to increase heat stress risk in the Brazilian Amazon. *Commun. Earth Environ.* **2**, 207 (2021).
40. Bastin, J.-F. *et al.* The global tree restoration potential. *Science* **365**, 76–79 (2019).
41. Griscom, B. W. *et al. Global Reforestation Potential Map*. https://doi.org/10.5281/zenodo.883444 (2017).
42. Agnan, Y., Le Dantec, T., Moore, C. W., Edwards, G. C. & Obrist, D. New Constraints on Terrestrial Surface–Atmosphere Fluxes of Gaseous Elemental Mercury Using a Global Database. *Environ. Sci. Technol.* **50**, 507–524 (2016).
43. Zhou, J. & Obrist, D. Global Mercury Assimilation by Vegetation. *Environ. Sci. Technol.* **55**, 14245–14257 (2021).
44. Pacyna, J. M. *et al.* Current and future levels of mercury atmospheric pollution on a global scale. *Atmos. Chem. Phys.* **16**, 12495–12511 (2016).
45. Steenhuisen, F. & Wilson, S. J. Development and application of an updated geospatial distribution model for gridding 2015 global mercury emissions. *Atmos. Environ.* **211**, 138–150 (2019).
46. COP26. *Glasgow Leaders' Declaration on Forests and Land Use*. https://ukcop26.org/glasgow-leaders-declaration-on-forests-and-land-use/ (2021).
47. Streets, D. G. *et al.* Global and regional trends in mercury emissions and concentrations, 2010–2015. *Atmospheric Environment* **201**, 417–427 (2019).
48. Lima, F. R. D. *et al.* Geochemistry signatures of mercury in soils of the Amazon rainforest biome. *Environmental Research* **215**, 114147 (2022).
49. Roulet, M., Lucotte, M., Canuel, R., Farella, N. & Courcelles, M. Increase in mercury contamination recorded in lacustrine sediments following deforestation in the central Amazon. 24 (2000).
50. Wohlgemuth, L. *et al.* Physiological and climate controls on foliar mercury uptake by European tree species. *Biogeosciences* **19**, 1335–1353 (2022).
51. Gelaro, R. *et al.* The Modern-Era Retrospective Analysis for Research and Applications, Version 2 (MERRA-2). *J. Clim.* **30**, 5419–5454 (2017).
52. Horowitz, H. M. *et al.* A new mechanism for atmospheric mercury redox chemistry: implications for the global mercury budget. *Atmos. Chem. Phys.* **17**, 6353–6371 (2017).
53. Schmidt, J. A. *et al.* Modeling the observed tropospheric BrO background: Importance of multiphase chemistry and implications for ozone, OH, and mercury. *J. Geophys. Res. Atmos.* **121**, 11,819-11,835 (2016).
54. Amos, H. M. *et al.* Gas-particle partitioning of atmospheric Hg(II) and its effect on global mercury deposition. *Atmos. Chem. Phys.* **12**, 591–603 (2012).

55. Liu, H., Jacob, D. J., Bey, I. & Yantosca, R. M. Constraints from ^{210}Pb and ^{7}Be on wet deposition and transport in a global three-dimensional chemical tracer model driven by assimilated meteorological fields. *J. Geophys. Res.* **106**, 12109–12128 (2001).
56. Wesely, M. L. Parameterization of surface resistances to gaseous dry deposition in regional-scale numerical models. *Atmos. Environ.* **23**, 1293–1304 (1989).
57. Wang, Y., Jacob, D. J. & Logan, J. A. Global simulation of tropospheric O_3-NO_x-hydrocarbon chemistry: 1. Model formulation. *J. Geophys. Res.* **103**, 10713–10725 (1998).
58. Lin, C.-J. & Pehkonen, S. O. The chemistry of atmospheric mercury: a review. *Atmos. Environ.* **33**, 2067–2079 (1999).
59. Fisher, J. A. *et al.* Sources, distribution, and acidity of sulfate–ammonium aerosol in the Arctic in winter–spring. *Atmos. Environ.* **45**, 7301–7318 (2011).
60. Zhang, L., Gong, S., Padro, J. & Barrie, L. A size-segregated particle dry deposition scheme for an atmospheric aerosol module. *Atmos. Environ.* **35**, 549–560 (2001).
61. Gibbs, H. K. Olson's Major World Ecosystem Complexes Ranked by Carbon in Live Vegetation: An Updated Database Using the GLC2000 Land Cover Product (NDP-017b). https://www.osti.gov/biblio/1389498, 2006. (2006).
62. Yuan, H., Dai, Y., Xiao, Z., Ji, D. & Shangguan, W. Reprocessing the MODIS Leaf Area Index products for land surface and climate modelling. *Remote Sens. Environ.* **115**, 1171–1187 (2011).
63. Strode, S. A. *et al.* Air-sea exchange in the global mercury cycle. *Global Biogeochem. Cycles* **21**, GB1017 (2007).
64. van der Werf, G. R. *et al.* Global fire emissions estimates during 1997–2016. *Earth Syst. Sci. Data* **9**, 697–720 (2017).
65. Selin, N. E. *et al.* Global 3-D land-ocean-atmosphere model for mercury: Present-day versus preindustrial cycles and anthropogenic enrichment factors for deposition. *Global Biogeochem. Cycles* **22**, GB2011 (2008).
66. Khan, T. R., Obrist, D., Agnan, Y., Selin, N. E. & Perlinger, J. A. Atmosphere-terrestrial exchange of gaseous elemental mercury: parameterization improvement through direct comparison with measured ecosystem fluxes. *Environ. Sci.: Processes Impacts* **21**, 1699–1712 (2019).
67. Verstraete, M. M. Radiation transfer in plant canopies: Transmission of direct solar radiation and the role of leaf orientation. *J. Geophys. Res.* **92**, 10985 (1987).
68. *Predicting soil erosion by water: a guide to conservation planning with the revised universal soil loss equation (RUSLE)*. (1997).
69. Borrelli, P. *et al.* An assessment of the global impact of 21st century land use change on soil erosion. *Nat Commun* **8**, 2013 (2017).
70. Lugato, E. *et al.* Soil erosion is unlikely to drive a future carbon sink in Europe. *Sci. Adv.* **4**, eaau3523 (2018).
71. Hecht, S. *et al. The Amazon in motion: Changing politics, development strategies, peoples, landscapes, and livelihoods*. 14.1-14.65 https://doi.org/10.55161/RWSX6527 (2021).
72. Carvalho, W. D. *et al.* Deforestation control in the Brazilian Amazon: A conservation struggle being lost as agreements and regulations are subverted and bypassed. *Perspectives in Ecology and Conservation* **17**, 122–130 (2019).
73. Michelazzo, P. A. M., Fostier, A. H., Magarelli, G., Santos, J. C. & de Carvalho, J. A. Mercury emissions from forest burning in southern Amazon. *Geophys. Res. Lett.* **37**, L09809 (2010).
74. Nobre, C. A. *et al.* Land-use and climate change risks in the Amazon and the need of a novel sustainable development paradigm. *Proc. Natl. Acad. Sci. U.S.A.* **113**, 10759–10768 (2016).

75. Dinerstein, E. *et al.* An Ecoregion-Based Approach to Protecting Half the Terrestrial Realm. *BioScience* **67**, 534–545 (2017).

Supplementary Information:

Land use change as an anthropogenic driver of mercury pollution

Authors

Aryeh Feinberg[a], Martin Jiskra[b], Pasquale Borrelli[c], Jagannath Biswakarma[b,d], and Noelle E. Selin[a,e]

[a] *Institute for Data, Systems, and Society, Massachusetts Institute of Technology, Cambridge, MA, USA*

[b] *Environmental Geosciences, University of Basel, Basel, Switzerland*

[c] *Department of Science, Roma Tre University, Rome, Italy*

[d] *Department of Water Resources and Drinking Water, Eawag, Dübendorf, Switzerland*

[e] *Department of Earth, Atmospheric, and Planetary Sciences, Massachusetts Institute of Technology, Cambridge, MA, USA*

Correspondence to: arifeinberg@gmail.com (A.F.); martin.jiskra@gmail.com (M.J.)

Section S1. Land-use scenarios

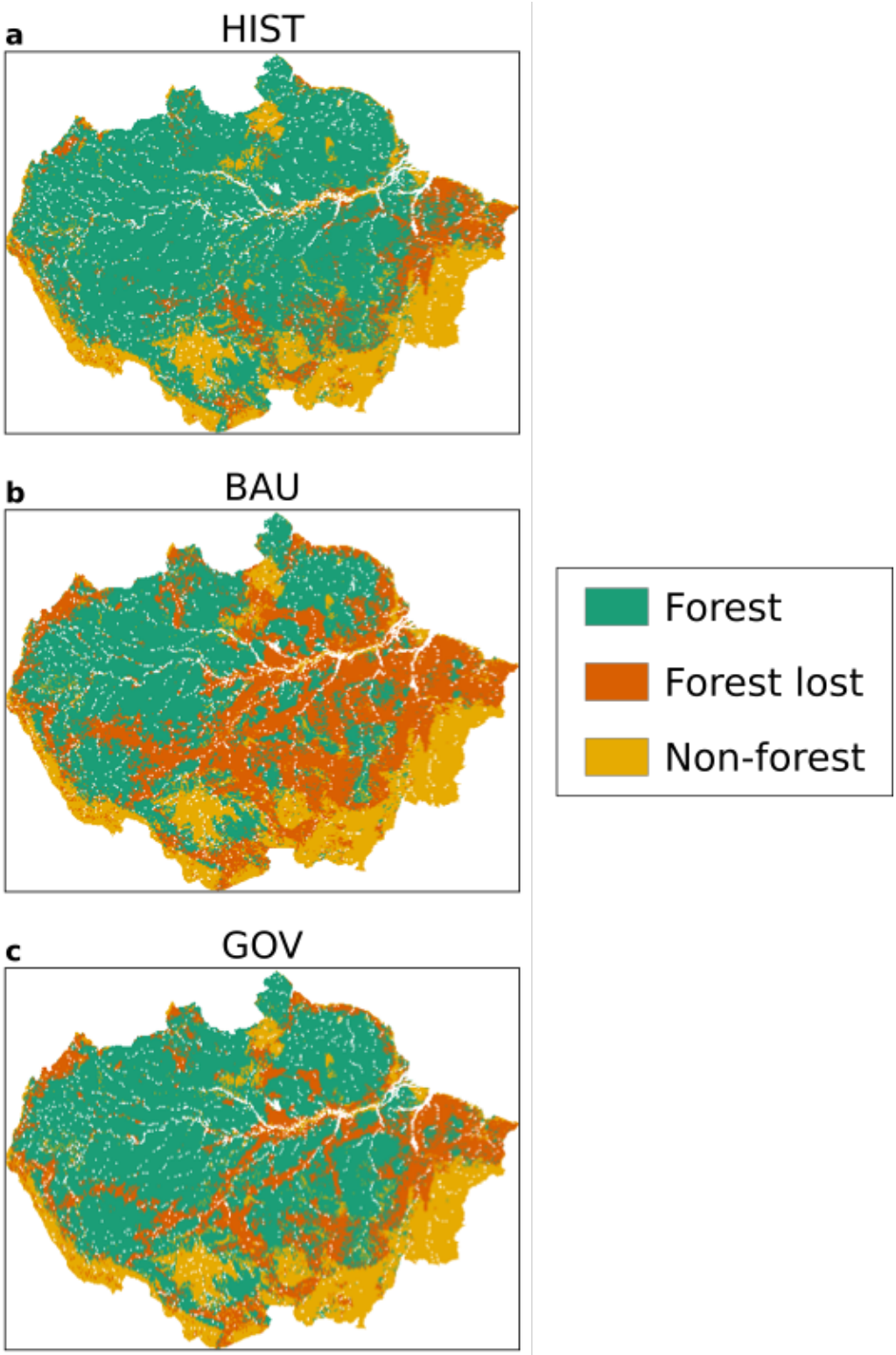

Figure S1. Map of the Amazon basin showing the area of forest, forest loss and rangeland and agriculture in **a.** HIST; and projections for 2050 in **b**. Business as Usual (BAU) and **c.** Governance (GOV) scenarios (replotted from Soares-Filho et al.[1] data).

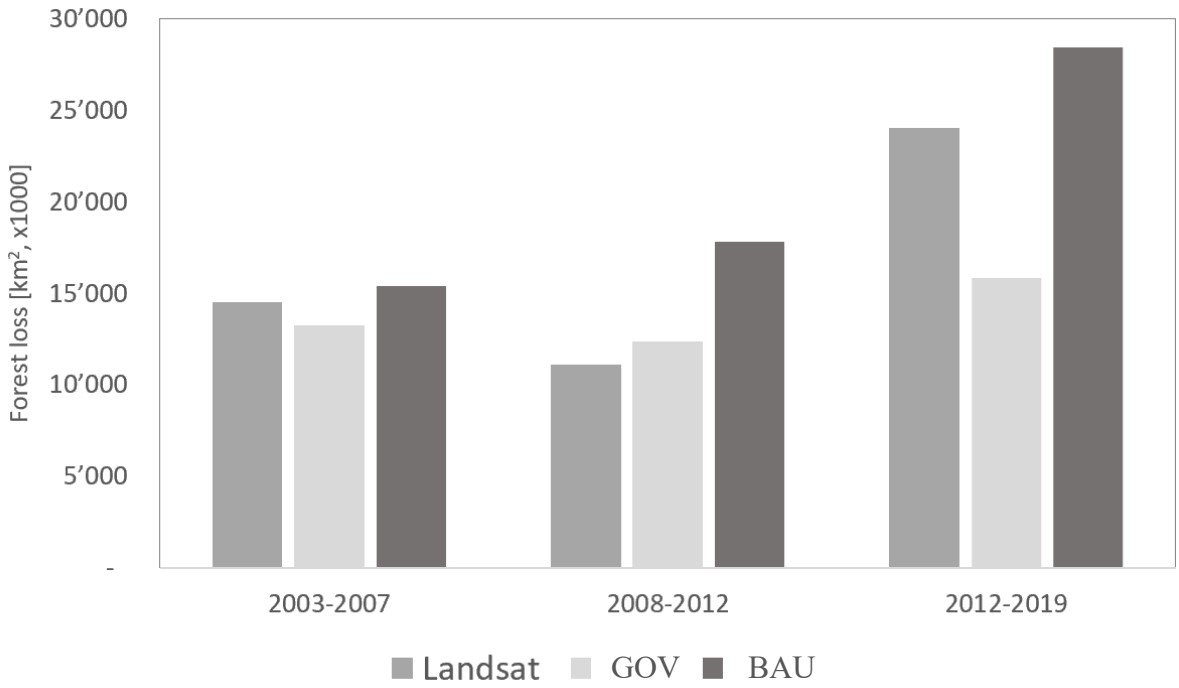

Figure S2. Comparison of deforestation from BAU and GOV scenarios with observational data from Landsat images.

Section S2. Soil emissions parametrization

We improved the model's parametrization of Hg^0 soil emissions by adopting a new formulation for the parametrization, suggested by Khan et al.[2]:

$$E_{\text{soil}} = aC^b R_g^c \qquad \text{(S1)}$$

where E_{soil} are soil emissions (ng m^{-2} h^{-1}), C is the concentration of Hg in soils (ng g^{-1}) , R_g is the solar radiation flux at the ground (W m^{-2}), and a, b, and c are coefficients.

As in Selin et al.[3], the solar radiation at ground (R_g) is determined by considering attenuation of the solar radiation flux (R_S) by shading from the overhead canopy, parametrized by the leaf area index (LAI):

$$R_g = R_S \exp\left(-\frac{\alpha \text{LAI}}{\cos\theta}\right) \qquad \text{(S2)}$$

where $\alpha = 0.5$, assuming extinction from a random angular distribution of leaves[4] and θ is the solar zenith angle.

We compiled several relevant observational constraints for the parametrization in Tables S1 and S2. Observational studies from the Amazon region suggest that deforestation has a large impact on soil emissions due to removal of canopy shading, showing factors of 1.8×, 6.7×, and >31× more emissions in forested compared to deforested land plots (Table S1). Observational studies from other regions find a similarly high sensitivity of soil

emissions to the presence of forest: open fields in China showed 6–10 times higher Hg emissions than forests[5] and logging in the US flipped the surface-air Hg^0 flux from net deposition to net emissions (–2.2 μg m^{-2} yr^{-1} to +5.5 μg m^{-2} yr^{-1})[6]. For extratropical grassland soil emissions, we use the compiled median values from Zhu et al.[7] and Agnan et al.[8]

We conducted a parameter sweep of *a*, *b,* and *c*, calculating globally-gridded soil emissions using annually averaged solar radiation data (Figure S3). Sensitivity simulations showed that the ratio of deforested to forested soil emissions in the Amazon (median value 6.7) can tune the exponent for the radiation term (*c* in Eq. S1), i.e., the response of emissions to canopy shading. The exponent for the soil concentration term (*b*) was tuned with the ratio of deforested Amazon soil emissions (Table S1) to extratropical grassland soil emissions from the Northern Hemisphere from two review studies[7,8] (overall Amazon to extratropical ratio of 5.3). Lastly, after these coefficients are tuned, the prefactor *a* is adjusted so that predicted annual mean emissions match the observed median magnitudes of Amazon deforested soil emissions (23 μg m^{-2} yr^{-1}) and extratropical grassland emissions (4.3 μg m^{-2} yr^{-1}).

Table S1. Literature review of available Hg^0 soil emission flux measurements from the Amazon region, differentiated by land cover type.

Reference	Location	Site	Deforested Hg^0 flux (μg m^{-2} yr^{-1})	Forested Hg^0 flux (μg m^{-2} yr^{-1})	Flux ratio (deforest:forest)
Magarelli and Foster[9]	Negro River Basin, Brazil	(1)	27 ± 9	0.6 ± 1.5	
		(2)	19	–1.0 ± 0.8	
		(3)	9.8 ± 0.7		
		Mean	18	–0.2	> 31[a]
Almeida et al.[10]	Rondônia, Brazil	(1)	79 ± 110	44 ± 18	1.8
Carpi et al.[11]	Acre, Brazil	(1)	19 ± 2	2.9 ± 0.8	6.7
		(2)	230[b]		
	Median		**23**	**1.8**	**6.7**

[a]upper limit calculated assuming the forested flux is equal to site (1), as site (2) shows negative overall flux

[b]this site was 2-months post-fire and soil temperatures were high; therefore, this flux is excluded from ratio calculations

Table S2. Observational constraints used to tune the soil emissions parametrization.

Constraint	Value	Reference	Coefficient constrained
Amazon deforested soil emissions (μg m^{-2} yr^{-1})	23	Table S1	*a*
Extratropical grassland soil emissions (μg m^{-2} yr^{-1})	4.3[†]	Zhu et al.[7]; Agnan et al.[8]	*a*
Ratio of Amazon to extratropical soil emissions	5.3	(23:4.3)	*b*
Ratio of deforested to forested Amazon soil emissions	6.7	Table S1	*c*

[†]average of grassland median Hg^0 fluxes from the two independent review studies

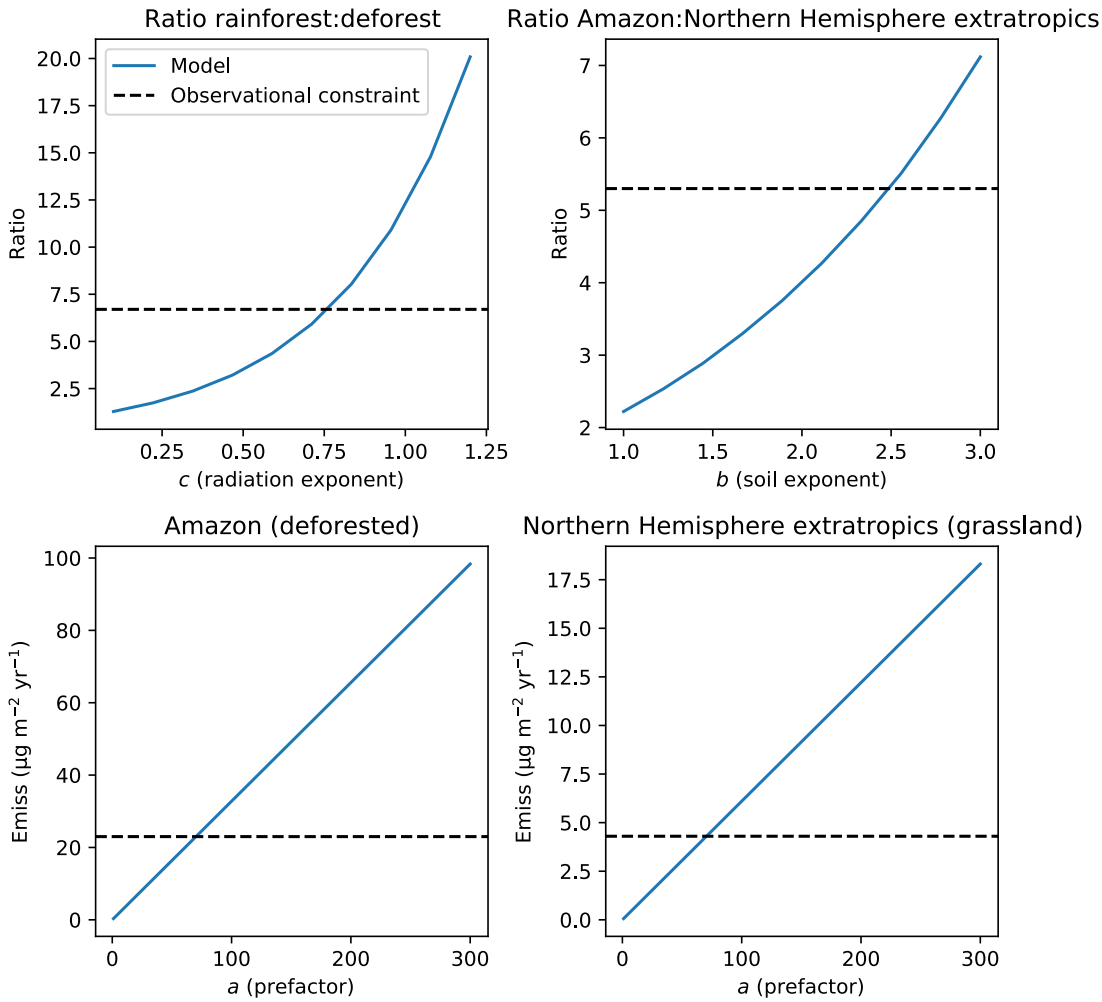

Figure S3. Parameter tuning (Eq. S2) to match observational constraints from Table S2.

The tuning procedure is illustrated in Figure S3, yielding best matches for a = 71, b = 2.5, and c = 0.76. We compare the gridded annual mean soil emissions from the previous soil emission parametrization (GEOS-Chem v12.8) and the current study (Eq. S1) in Figure S4. Global annual mean soil Hg^0 emissions in the new parametrizations (954 Mg yr^{-1}) is similar to the predictions from two GEOS-Chem studies[12,13] using the previous parametrization: 860 ± 440 Mg yr^{-1} and 910 Mg yr^{-1}. The spatial distribution of emissions (Figure S4) shows a decrease in vegetated regions (e.g., the Amazon and Congo rainforests) and an increase in regions with high soil Hg concentrations (e.g., eastern China).

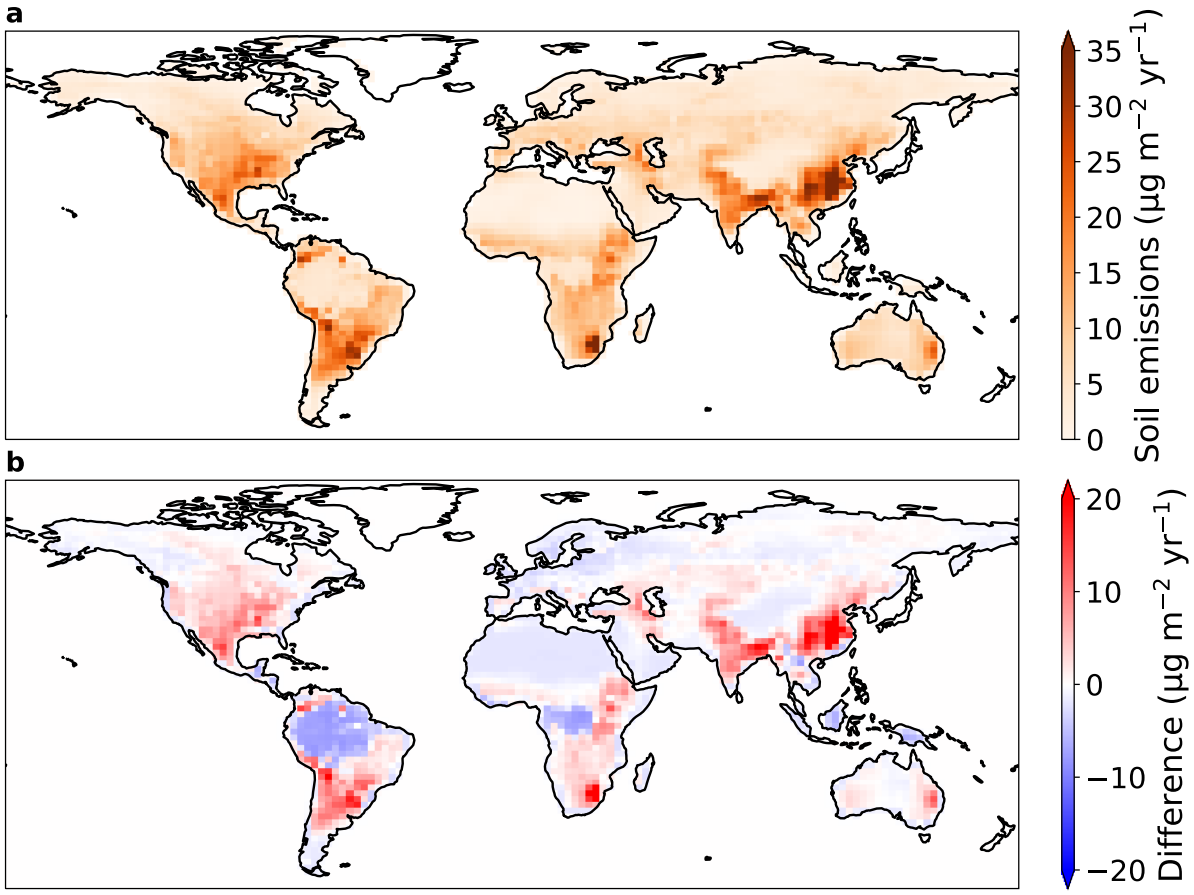

Figure S4. a. Annual mean soil emissions of Hg^0 with the new parametrization. **b.** Difference between new and old (GEOS-Chem v12.8) soil emissions parametrizations (new minus old).

Section S3. Leaf area index (LAI) maps for the scenarios

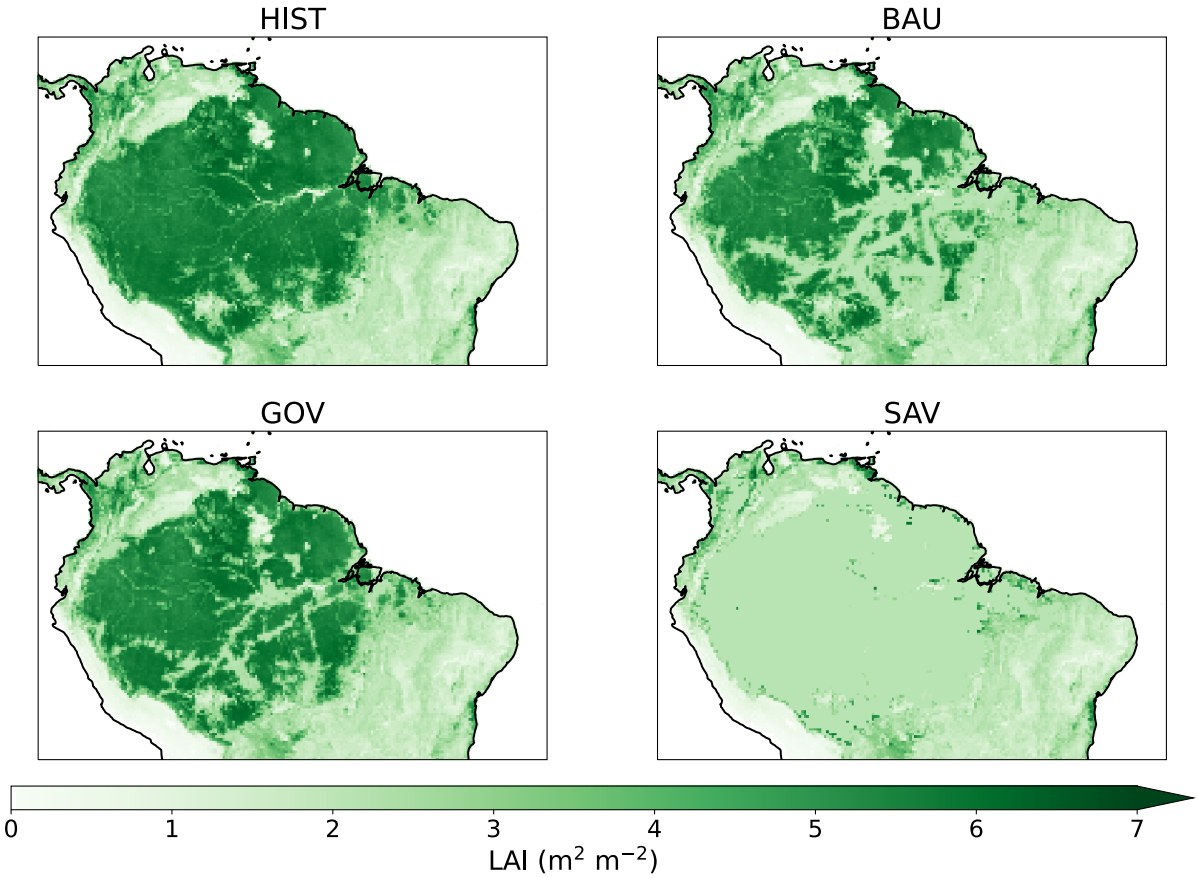

Figure S5. Annual mean leaf area index (LAI) maps for the Amazon deforestation scenarios at 0.25 × 0.25° resolution.

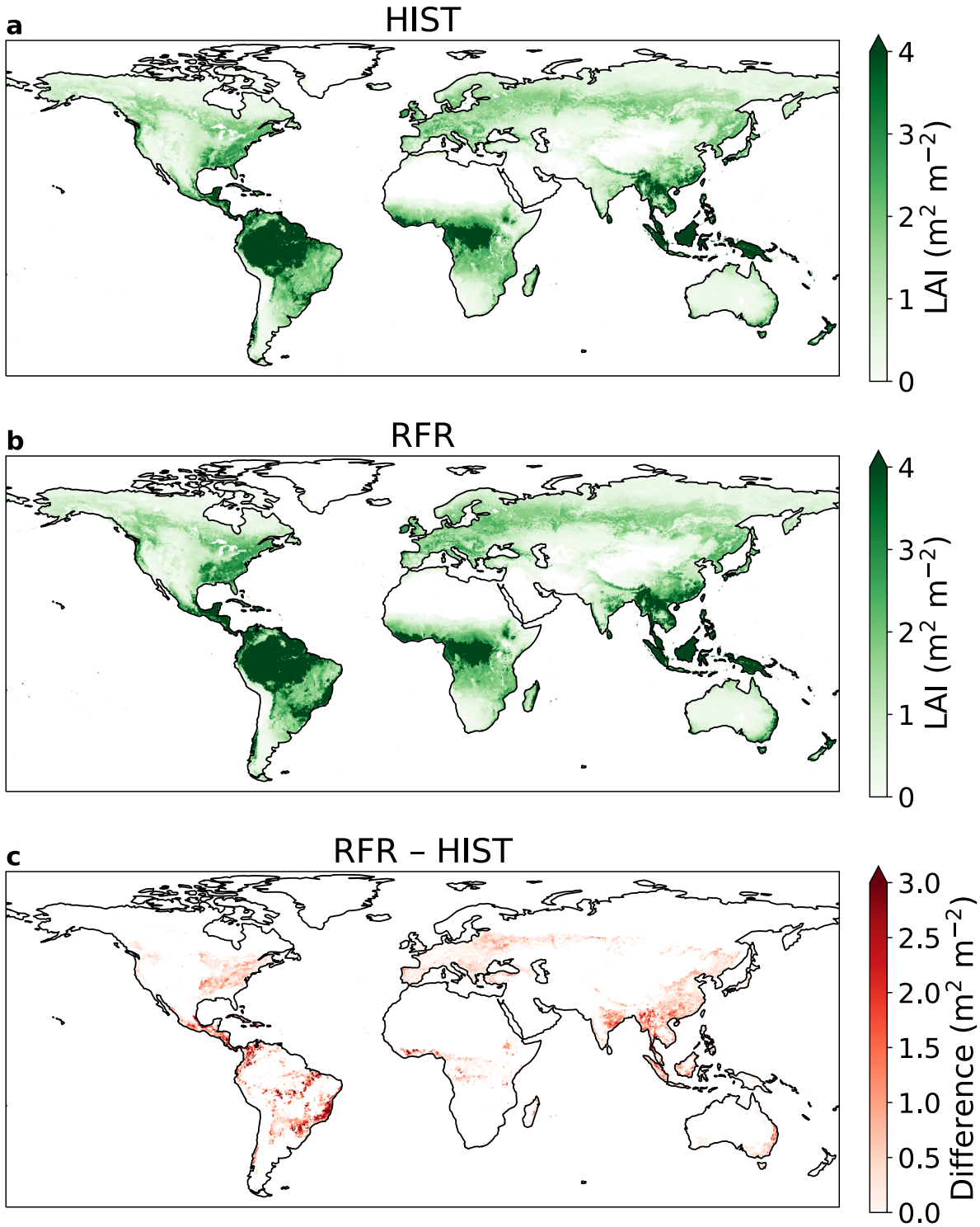

Figure S6. Annual mean leaf area index (LAI) maps at 0.25 × 0.25° resolution for: **a.** HIST **b.** Reforestation scenario (RFR) **c.** Difference between RFR and HIST.

Section S4. Impacts on atmospheric Hg concentrations

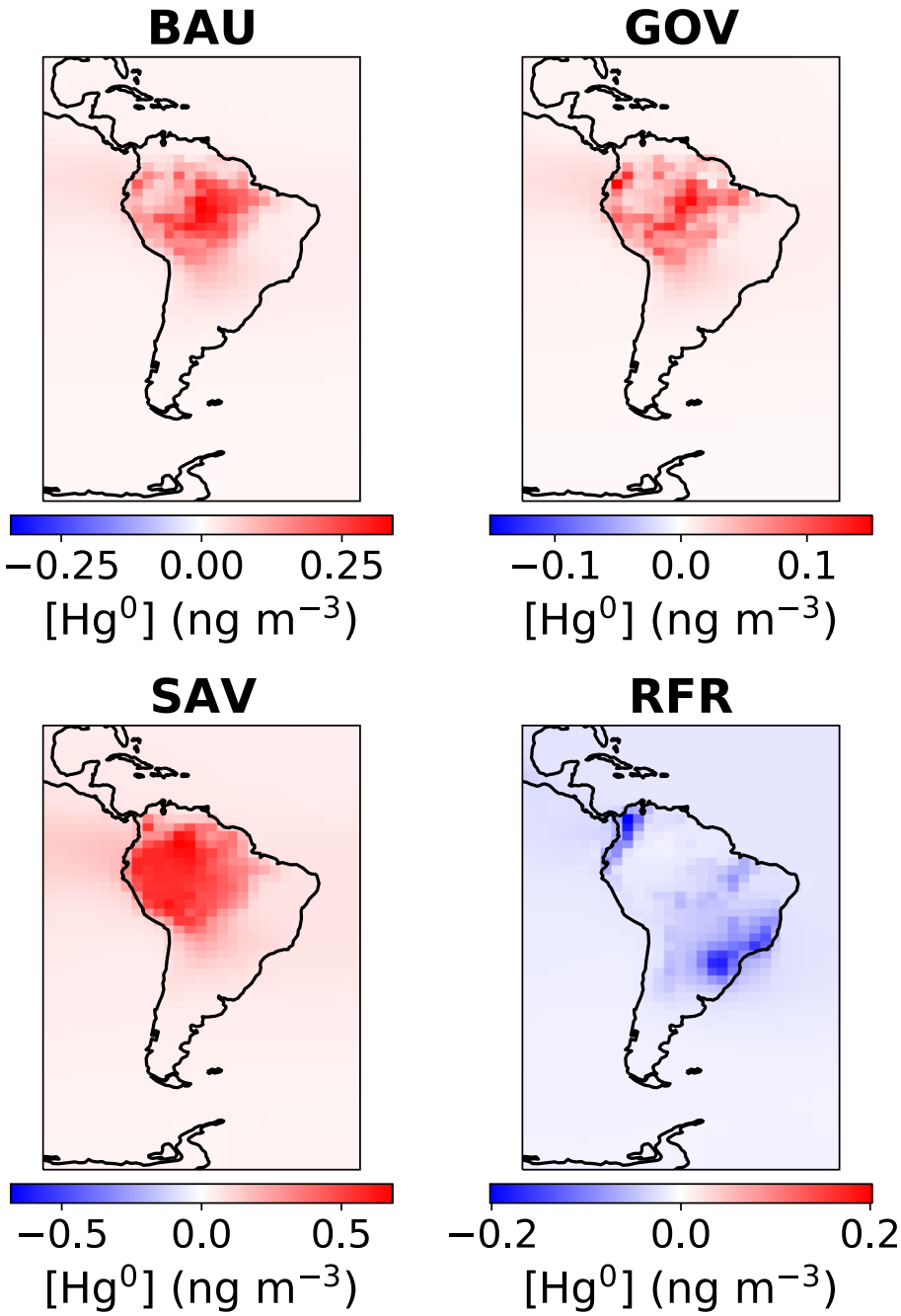

Figure S7. Annual mean differences in simulated atmospheric Hg^0 concentration at the surface between scenarios and the HIST reference simulation.

Section S5. Calculation of C-Factor for erosion modelling

The land cover and management factor (C-factor) measures the combined effect of vegetation cover and cropping system variables on the soil erosion process. Two datasets are used to calculate the C-Factor: 1) the land use scenario maps from Soares-Filho et al.[13]; 2) the MODIS MOD44B Vegetation Continuous Fields product (VCF). As we focus our analysis on comparing the forest coverage in the years 2003 and 2050, the baseline vegetation condition is given by the average VCF values over the years 2000, 2001 and 2002. The C-factor for noncropland areas (C_{nc}) is estimated in two steps. First, a preliminary C-factor (C_p) not considering tree cover is calculated as:

$$C_p = C_{min} + \left((C_{max} - C_{min})\,\mathrm{NVS}\right) \qquad \text{(S3)}$$

where the C_{min} (0.01) and C_{max} (0.15) express the potential range in C-factor values for dense to sparse grassland cover. NVS (non-vegetated surface) is spatially defined using the MODIS MOD44B VCF data normalized to a range from 0 to 1 and describes the percentage of ground covered by any vegetation type. For the NVS, the C-factor is set to 0.5. Within the next step, the final land cover and management C-factor for non-croplands (C_{nc}) is computed including the tree coverage (TC) defined using the MODIS MOD44B VCF normalized to range from 0 to 1:

$$C_{nc} = C_{p\,min} + \left(\left(C_{p\,max} - C_{p\,min}\right)\mathrm{TC}\right) \qquad \text{(S4)}$$

where the $C_{p\,min}$ and $C_{p\,max}$ values are set to 0.0001 (100% canopy cover) and 0.009 (sparse forest vegetation).

While the deforestation scenarios proposed by Soares-Filho et al.[1] provide a spatial quantification of the forest losses between 2003 and 2050, the annual shares of conversion from forest to grassland or cropland are separate from the annual projection of the Land-Use Harmonization (LUH2) data[14], which provides fractional land-use patterns (850-2100) at 0.25° × 0.25° resolution. The downscaling of the LUH2 fractional cropland and grassland data from 0.25° × 0.25° resolution to the 250 m × 250 m resolution of the erosion model is performed through a probabilistic land use allocation scheme based on classification rules applied to auxiliary information (i.e., a crop suitability index, more detail in Borrelli et al.[15]). Finally, the C-factor of the cropland is defined at sub-national administrative level (Global Administrative Unit Levels) based on the Food and Agriculture Organization's (FAO) FAOSTAT database, which allowed to statistically describe typical crop rotations in each region. The C-factor of the croplands ranges from 0.131 (Northern Suriname) to 0.332 (Northeast Brazil).

SI References

1. Soares-Filho, B. S. *et al.* Modelling conservation in the Amazon basin. *Nature* **440**, 520–523 (2006).
2. Khan, T. R., Obrist, D., Agnan, Y., Selin, N. E. & Perlinger, J. A. Atmosphere-terrestrial exchange of gaseous elemental mercury: parameterization improvement through direct comparison with measured ecosystem fluxes. *Environ. Sci.: Processes Impacts* **21**, 1699–1712 (2019).
3. Selin, N. E. *et al.* Global 3-D land-ocean-atmosphere model for mercury: Present-day versus preindustrial cycles and anthropogenic enrichment factors for deposition. *Global Biogeochem. Cycles* **22**, GB2011 (2008).
4. Verstraete, M. M. Radiation transfer in plant canopies: Transmission of direct solar radiation and the role of leaf orientation. *J. Geophys. Res.* **92**, 10985 (1987).
5. Zhou, J., Wang, Z., Zhang, X., Driscoll, C. T. & Lin, C.-J. Soil–atmosphere exchange flux of total gaseous mercury (TGM) at subtropical and temperate forest catchments. *Atmos. Chem. Phys.* **20**, 16117–16133 (2020).
6. Eckley, C. S., Eagles-Smith, C., Tate, M. T. & Krabbenhoft, D. P. Surface-air mercury fluxes and a watershed mass balance in forested and harvested catchments. *Environmental Pollution* **277**, 116869 (2021).
7. Zhu, W. *et al.* Global observations and modeling of atmosphere–surface exchange of elemental mercury: a critical review. *Atmos. Chem. Phys.* **16**, 4451–4480 (2016).
8. Agnan, Y., Le Dantec, T., Moore, C. W., Edwards, G. C. & Obrist, D. New Constraints on Terrestrial Surface–Atmosphere Fluxes of Gaseous Elemental Mercury Using a Global Database. *Environ. Sci. Technol.* **50**, 507–524 (2016).
9. Magarelli, G. & Fostier, A. Influence of deforestation on the mercury air/soil exchange in the Negro River Basin, Amazon. *Atmos. Environ.* **39**, 7518–7528 (2005).
10. Almeida, M. D., Marins, R. V., Paraquetti, H. H. M., Bastos, W. R. & Lacerda, L. D. Mercury degassing from forested and open field soils in Rondônia, Western Amazon, Brazil. *Chemosphere* **77**, 60–66 (2009).
11. Carpi, A., Fostier, A. H., Orta, O. R., dos Santos, J. C. & Gittings, M. Gaseous mercury emissions from soil following forest loss and land use changes: Field experiments in the United States and Brazil. *Atmos. Environ.* **96**, 423–429 (2014).
12. Song, S. *et al.* Top-down constraints on atmospheric mercury emissions and implications for global biogeochemical cycling. *Atmos. Chem. Phys.* **15**, 7103–7125 (2015).

13. Horowitz, H. M. *et al.* A new mechanism for atmospheric mercury redox chemistry: implications for the global mercury budget. *Atmos. Chem. Phys.* **17**, 6353–6371 (2017).
14. Hurtt, G. C. *et al.* Harmonization of global land use change and management for the period 850–2100 (LUH2) for CMIP6. *Geosci. Model Dev.* **13**, 5425–5464 (2020).
15. Borrelli, P. *et al.* Land use and climate change impacts on global soil erosion by water (2015-2070). *Proc. Natl. Acad. Sci. U.S.A.* **117**, 21994–22001 (2020).